



**HAL**  
open science

# Wave Interaction of Reverse-Fault Rupture With Free Surface: Numerical Analysis of the Dynamic Effects and Fault Opening Induced by Symmetry Breaking

A. Scala, G. Festa, Jean-Pierre Vilotte, S. Lorito, F. Romano

► **To cite this version:**

A. Scala, G. Festa, Jean-Pierre Vilotte, S. Lorito, F. Romano. Wave Interaction of Reverse-Fault Rupture With Free Surface: Numerical Analysis of the Dynamic Effects and Fault Opening Induced by Symmetry Breaking. *Journal of Geophysical Research: Solid Earth*, 2019, 124, pp.1743-1758. 10.1029/2018JB016512 . insu-03586658

**HAL Id: insu-03586658**

**<https://insu.hal.science/insu-03586658>**

Submitted on 24 Feb 2022

**HAL** is a multi-disciplinary open access archive for the deposit and dissemination of scientific research documents, whether they are published or not. The documents may come from teaching and research institutions in France or abroad, or from public or private research centers.

L'archive ouverte pluridisciplinaire **HAL**, est destinée au dépôt et à la diffusion de documents scientifiques de niveau recherche, publiés ou non, émanant des établissements d'enseignement et de recherche français ou étrangers, des laboratoires publics ou privés.

Copyright

# JGR Solid Earth

## RESEARCH ARTICLE

10.1029/2018JB016512

### Key Points:

- Symmetry breaking from free surface/rupture interaction may enhance slip, ground motion, and tsunamigenic potential of shallow ruptures
- Rupture dynamics deviates from classical linear elastic fracture mechanics: inertial effects in the energy balance and shallow opening
- The effects of the interaction are strongly sensitive to the friction level; the higher the friction, the more important the interaction

### Supporting Information:

- Supporting Information S1

### Correspondence to:

A. Scala,  
antonio.scala@ingv.it

### Citation:

Scala, A., Festa, G., Vilotte, J.-P., Lorito, S., & Romano, F. (2019). Wave interaction of reverse-fault rupture with free surface: Numerical analysis of the dynamic effects and fault opening induced by symmetry breaking. *Journal of Geophysical Research: Solid Earth*, 124, 1743–1758. <https://doi.org/10.1029/2018JB016512>

Received 7 AUG 2018

Accepted 27 DEC 2018

Accepted article online 28 DEC 2018

Published online 9 FEB 2019

©2018. American Geophysical Union.  
All Rights Reserved.

## Wave Interaction of Reverse-Fault Rupture With Free Surface: Numerical Analysis of the Dynamic Effects and Fault Opening Induced by Symmetry Breaking

A. Scala<sup>1,2</sup> , G. Festa<sup>1</sup> , J.-P. Vilotte<sup>3</sup>, S. Lorito<sup>2</sup> , and F. Romano<sup>2</sup> 

<sup>1</sup>Dipartimento di Fisica “Ettore Pancini”, Università degli studi di Napoli Federico II, Naples, Italy, <sup>2</sup>Istituto Nazionale di Geofisica e Vulcanologia, Rome, Italy, <sup>3</sup>Institut de Physique du Globe de Paris, CNRS-INSU, Paris, France

**Abstract** Several great earthquakes occur on thrust faults along both subduction and continental collision zones. These events often feature a large shallow slip patch, an asymmetric pattern for the ground motion, and the static deformation between the hanging wall and footwall of the fault. From a mechanical point of view, this asymmetry can be partially explained taking into account the interaction between the fault and the seismic radiation emitted during rupture propagation and stored in the hanging wall in the vicinity of the free surface. We numerically investigate the rupture dynamics along a thrust dipping fault impacting onto the free surface at a dip angle of  $\delta = 20^\circ$ , in a 2-D elastic model. We show how the wave interaction of the rupture with the free surface leads to a breaking of the reflection symmetry. Compared to a rupture propagating in an infinite medium, this interaction enhances the slip rate in the updip direction as an effect of the coupling between slip and normal traction around the crack front. The breaking of symmetry leads to sizeable acceleration of the rupture toward asymptotic speed with inertia acquisition, and dependence of the rupture dynamics on the level of friction along the interface might produce an interface opening over a finite length in the vicinity of the surface. We finally explore how the wave interaction drives amplification and asymmetry of the shallow slip and the vertical displacement at the surface. The described effects should be considered in various numerical approaches and in interpretation of geophysical observations.

## 1. Introduction

Understanding the dynamics of a spontaneously propagating frictional rupture along a thrust fault embedded in elastic media is a long-standing problem with important theoretical and practical implications in the context of active collision and subduction zones, where large earthquakes predominantly occur.

Noteworthy observations associated with these earthquakes show large shallow slip and/or an asymmetric ground motion in the hanging wall in the vicinity of the fault—with much larger strong motion and possibly inelastic deformation—that may trigger significant structural damage, and/or destructive tsunamis, such as for the 1994  $M_w$  6.7 Northridge earthquake (Abrahamson & Sommerville, 1996), the 1999  $M_w$  7.7 Chi-Chi earthquake (Zhang et al., 2008), the 2004  $M_w$  9.2 Sumatra earthquake (Shearer & Bürgmann, 2010), the 2011  $M_w$  9.1 Tohoku earthquake (Lay, 2018; Satake et al., 2013), and the 2013  $M_w$  7.7 Balochistan earthquake (Vallage et al., 2015).

Numerical investigations (Ma & Archuleta, 2006; Murphy et al., 2016; Nielsen, 1998; Oglesby et al., 1998, 2000; Uenishi, 2015) of spontaneous rupture propagation along a thrust fault separating two identical elastic materials have shown that slip-induced normal traction variations and interaction of the rupture with the free surface through seismic waves enhance the rupture propagation in the updip direction with large slip close to the surface. This wave interaction also enhances the amount of radiated energy along the forward rupture direction and with an asymmetry in the ground motion and the surface deformation (Brune, 1996). This has been interpreted as resulting from trapped waves in the hanging wall together with a geometrically induced effective compliance of the hanging wall. Material asymmetry between the hanging wall and the footwall has also been numerically investigated (Ma & Beroza, 2008; Kozdon & Dunham, 2013; Lotto et al., 2017), in particular in the context of subduction zones. Directivity of the rupture propagation induced by the bimaterial interface is shown to further favor the updip rupture propagation and to allow the penetration of the rupture also in velocity-strengthening shallow portions of the frictional interface close to the

surface. The bimaterial effect increases the strength drop along the interface, together with the ground motion asymmetry and slip concentration close to the surface. However, when a dynamically induced inelastic effect is included in the hanging wall (Ma, 2012; Ma & Hirakawa, 2013), lower radiated energy and rupture velocity, together with a smaller directivity effect, are predicted as observed for shallow subduction earthquakes

Laboratory thrust-fault experiments combined with linear elastic numerical simulations (e.g., Brune, 1996; Shi et al., 1998) have also provided further insights on the implication of geometrical and material symmetry breaking on subshear and supershear rupture propagation. In particular, experiments and numerical simulations of Gabuchian et al. (2014, 2017) reveal the existence of a geometrically induced torque mechanism in the hanging wall. This mechanism reduces the normal traction along the shallow portion of the interface. The weakening of the interface promotes dynamic rupture propagation up to the surface where spontaneous fault opening can be triggered. At this stage, a supershear propagation of the rupture downdip is nucleated, trailed by a sliding pulse propagating at Rayleigh wave speed. Fault opening is supported by early linear elastic fracture mechanics analysis (Erdogan & Arin, 1975; Rudnicki & Wu, 1995; Brune, 1996).

In a different context, recent analytic linear stability analysis (Aldam et al., 2016; Brener et al., 2016) shows that geometrical symmetry breaking and interaction with the domain boundary have an important implication on the stability of a finite-height elastic layer sliding atop of a semi-infinite elastic half-space along a velocity-strengthening frictional interface. The sliding stability is controlled by slip-induced normal traction variations and by the absolute level of friction along the interface, both of which depend on the degree of geometrical asymmetry. These studies provide new insights on the implication of symmetry breaking on the rupture dynamics when the rupture interacts with boundaries.

Finally, laboratory experiments (Fineberg & Bouchbinder, 2015; Goldman et al., 2010), and analytical studies (Marder, 1991; Zhou & Shioya, 1996) have shed light on interactions of reflected waves with the rupture when the system has a reflection symmetry across the interface. For a rupture propagating in a long elastic strip, effective inertial dynamics is inherited from the interaction of the rupture with the strip boundaries, mediated by the waves radiated during the rupture and reflected at the boundary, giving rise to an acceleration-dependent energy release rate (with a velocity-dependent effective mass) and a memory effect. This is in contrast with a rupture propagating in an infinite medium for which rupture front dynamics is not inertial; that is, the rupture front behaves as a massless particle where acceleration plays no role. When rupture interacts with boundaries, effective inertia dynamics control the rupture acceleration toward the asymptotic propagation speed.

Spontaneous rupture dynamics along reverse-fault frictional interface is thus a not yet well understood complex problem. The effect of the interaction between rupture and waves generated at the free surface depends on the specific wave type and on the dynamic stage of the rupture at the time of the interaction. The lack of symmetry, even when the interface separates two identical materials, leads to a coupling between the interfacial slip and the normal traction variations with implications on the rupture dynamics and directivity, such as memory and inertial effects, opening, and a dependence on the frictional level, that need to be finely addressed.

In this paper, we use extensive numerical simulations to address spontaneous dynamic rupture propagation along a slip-weakening frictional interface separating two identical elastic materials. The goal is to explore the implications of the geometric symmetry breaking and of the interaction between the rupture and seismic waves generated at the free surface on the rupture dynamics and the induced surface deformation. This is done through a systematic numerical comparison with a symmetric fault interface. Specifically, we finely analyze sliding-induced normal traction variations during the spontaneous rupture propagation due to reflected body and Rayleigh waves from the free surface and their effect on the rupture dynamics. We then investigate effective inertial dynamics occurring during the rupture acceleration toward the asymptotic speed and explore the opening effect near the surface and the influence of the absolute frictional level on the energy release rate under the condition of symmetry breaking.

The paper is organized as follows. The numerical method and the geometrical setup of the simulations are described in section 2; the results are presented in section 3 through systematic comparisons between the free surface and the unbounded medium cases, for different nucleation depths and different levels of friction.

## 2. Numerical Method and Setup

### 2.1. Mechanical Method

We numerically solve the elastodynamic equation in each point  $\mathbf{x}$  of the elastic domain and for each time  $t$  to describe the propagation of seismic waves in an elastic medium:

$$\begin{cases} \rho(\mathbf{x})\dot{\mathbf{v}}(\mathbf{x}, t) = \vec{\nabla} \cdot \boldsymbol{\sigma}(\mathbf{x}, t) \\ \dot{\boldsymbol{\sigma}}(\mathbf{x}, t) = \mathbf{c}(\mathbf{x}) : \vec{\nabla} \mathbf{v}(\mathbf{x}, t) \end{cases} \quad (1)$$

Here  $\rho(\mathbf{x})$  is the material density,  $\mathbf{v}(\mathbf{x}, t)$  is the particle velocity,  $\boldsymbol{\sigma}(\mathbf{x}, t)$  is the Cauchy stress tensor, and  $\mathbf{c}(\mathbf{x})$  is the fourth-order Hooke tensor for linear elasticity. The dot denotes time derivative. We impose that the traction  $\mathbf{T} = \boldsymbol{\sigma} \cdot \mathbf{n}$  is 0 at the free surface, where  $\mathbf{n}$  is the outward normal to the free surface. We apply contact and friction conditions at the zero-thickness interface representing the fault to dynamically model the rupture propagation. The traction  $\mathbf{T}$  is imposed to be continuous across the interface, whereas the kinematic quantities can be discontinuous. Slip and slip rate are computed through a domain decomposition along the interface separating the two subdomains on the two sides of the fault interface, hereinafter referred by the subscripts 1 and 2. We then separately solve equation (1) for the two subdomains. For a point  $\boldsymbol{\xi}$  on the interface, we define the interfacial slip and slip rate as  $\delta \mathbf{u}(\boldsymbol{\xi}, t) = \mathbf{u}_2(\boldsymbol{\xi}, t) - \mathbf{u}_1(\boldsymbol{\xi}, t)$  and  $\delta \mathbf{v}(\boldsymbol{\xi}, t) = \mathbf{v}_2(\boldsymbol{\xi}, t) - \mathbf{v}_1(\boldsymbol{\xi}, t)$ , respectively.

We assume a Signorini contact condition along the interface:

$$\begin{cases} \delta u^n(\boldsymbol{\xi}, t) \geq 0 \\ T^n(\boldsymbol{\xi}, t) \leq 0 \\ \delta u^n(\boldsymbol{\xi}, t) \cdot T^n(\boldsymbol{\xi}, t) = 0 \end{cases} \quad (2)$$

where the superscript  $n$  refers to the component of the fields normal to the interface. The normal vector is defined as the outward normal to the fault side belonging to medium 1. According to equation (2), when the total normal traction is compressive, the two blocks are in contact, whereas when the normal traction perturbation is equal to the initial compressive normal traction (total normal traction  $T^n = 0$ ), the interface behaves as a free surface; in this case the two lips of the fault are allowed to separate from each other and a local opening of the interface occurs.

When the two sides of the interface are in contact, the frictional sliding is modeled by imposing the Coulomb condition:

$$\begin{cases} (|\mathbf{T}^t(\boldsymbol{\xi}, t)| - C(\boldsymbol{\xi}) + \mu T^n(\boldsymbol{\xi}, t)) \cdot |\delta \mathbf{v}^t(\boldsymbol{\xi}, t)| = 0 \\ (|\mathbf{T}^t(\boldsymbol{\xi}, t)| - C(\boldsymbol{\xi}) + \mu T^n(\boldsymbol{\xi}, t)) \leq 0 \\ \mathbf{T}^t(\boldsymbol{\xi}, t) \cdot \delta \mathbf{v}^t(\boldsymbol{\xi}, t) = |\mathbf{T}^t(\boldsymbol{\xi}, t)| |\delta \mathbf{v}^t(\boldsymbol{\xi}, t)| \end{cases} \quad (3)$$

The superscript  $t$  now represents the tangential direction with respect to the interface, and  $C$  is the cohesion of the interface, which goes to 0 at the free surface. We assume a linear slip weakening behaviour of the friction coefficient  $\mu$  during the sliding; it linearly decreases from a static level  $\mu_s$  to the dynamic one  $\mu_d$  over a characteristic slip distance  $D_c$ ; beyond  $D_c$  the friction is maintained constant to the dynamic level (Ida, 1972). Finally,  $-\mu(\delta \mathbf{u}^t) T^n$  is the frictional strength.

The first condition in (3) indicates that the frictional sliding ( $|\delta \mathbf{v}^t| \neq 0$ ) occurs when the tangential traction lies on the surface of the Coulomb cone ( $|\mathbf{T}^t| - C + \mu T^n = 0$ ); when the interface is stick, the traction is inside the Coulomb cone (the second equation in (3)). The final condition describes the colinearity between the tangential traction and the slip rate, which is automatically insured in the 2-D models presented in this work.

Physical quantities are normalized to provide a general framework for the results. In particular, the slip is normalized by the critical slip weakening distance  $\delta \tilde{\mathbf{u}} = \delta \mathbf{u} / D_c$ . The traction  $\mathbf{T}$  is normalized as  $\tilde{\mathbf{T}} = \mathbf{T} / \Delta \sigma_0$  assuming a reference stress drop  $\Delta \sigma_0$  as the maximum value of the initial stress drop on the fault, that is,  $\max[\tau_0(x) - \mu_d \cdot \sigma_n^0(x)]$  with  $\tau_0$ ,  $\mu_d$ , and  $\sigma_n^0$  being the initial shear traction, the dynamic friction coefficient,

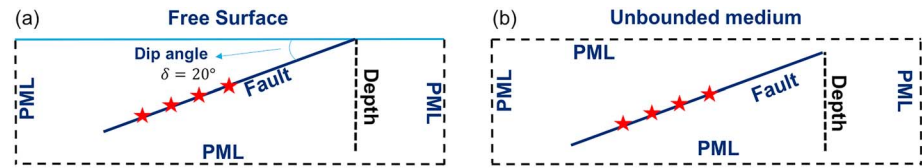


**Figure 1.** Geometrical setup for the numerical simulations. (a) A thrust planar fault impacts the free surface with a dip angle  $\delta = 20^\circ$ . On the other three boundaries, perfectly matched layer (PML) conditions are imposed. The red stars on the fault depict the different nucleation depths. (b) The same fault is embedded in an infinite medium, obtained surrounding the domain with PMLs.

and the initial normal traction, respectively. The distance  $z$  and the time  $t$  are normalized as  $\tilde{z} = \frac{\Delta\sigma_0}{G \cdot D_c} z$  and  $\tilde{t} = \frac{V_s \cdot \Delta\sigma_0}{G \cdot D_c} t$ , respectively, where  $G$  is the shear modulus and  $V_s$  is the  $S$  wave velocity. Accordingly, all the rupture and wave speeds are normalized by the  $S$  wave velocity, and the dimensionless slip rate is derived by the normalization of slip and time.

## 2.2. Geometrical Setup and Numerical Model

We numerically model the fault as a planar interface intersecting the free surface with a dip angle of  $20^\circ$  (Figure 1a); the rupture is nucleated at different depths (red stars in Figure 1) and propagates under different absolute levels of friction along the interface.

The numerical approximation is based on the spectral element method (Komatitsch & Vilotte, 1998) accounting for nonsmooth contact and friction conditions (Festa & Vilotte, 2006; Scala et al., 2017). The spatial approximation is based on an irregular quadrangular element mesh. The elements naturally follow the shape of the wedge between the free surface and the shallow part of the fault (Figure S1 in the supporting information) without generating any mesh-related artifact. We use  $9 \times 9$  Gauss-Lobatto-Legendre collocation points within each element, and the size of the elements is chosen to ensure at least 5 points for the minimum wavelength during the rupture propagation (Komatitsch & Vilotte, 1998) and 4 points in the process zone.

The time integration is performed through a second-order forward scheme. The stability of the time scheme is ensured by a Courant number of about 0.04.

To numerically mimic an infinite half-space, perfectly matched layers (PMLs) are used on the three other edges of the model (Festa et al., 2005; Festa & Vilotte, 2005); this allows to strongly reduce spurious reflections from the boundaries of the numerical domain. We evaluate the effect of the interaction between the rupture and the free surface through additional numerical simulations performed in an infinite unbounded medium with the same fault geometry, where the free surface is replaced by a PML (Figure 1b). We verified that the fault is far enough from the PMLs avoiding any mesh-dependent numerical artifacts.

## 2.3. Initial Conditions

The interface normal traction is imposed to monotonically increase with depth along the dipping fault interface to mimic the lithostatic loading as in similar studies (Huang et al., 2012).

The linear slip weakening friction parameters, that is, the static ( $\mu_s$ ) and dynamic ( $\mu_d$ ) friction coefficients, and the initial strength excess parameter  $s = (\mu_s T_0^n - T_0^t) / (T_0^t - \mu_d T_0^n)$  are assumed to be uniform along the interface. In the above formula the subscript 0 refers to the initial value of the field.

As such, the shear traction, the initial stress, and the strength drop also increase with depth with the maximum stress drop at the bottom of the interface. An interface cohesion  $C$  is imposed at about 10% of the maximum stress drop and goes to 0 at the free surface.

To analyze the implication of frictional level on the rupture dynamics, and on its interaction with the waves reflected by the surface, different sets of friction values have been investigated. However, the same initial normal traction profile is imposed independently of the friction level. We thus rescale the initial shear

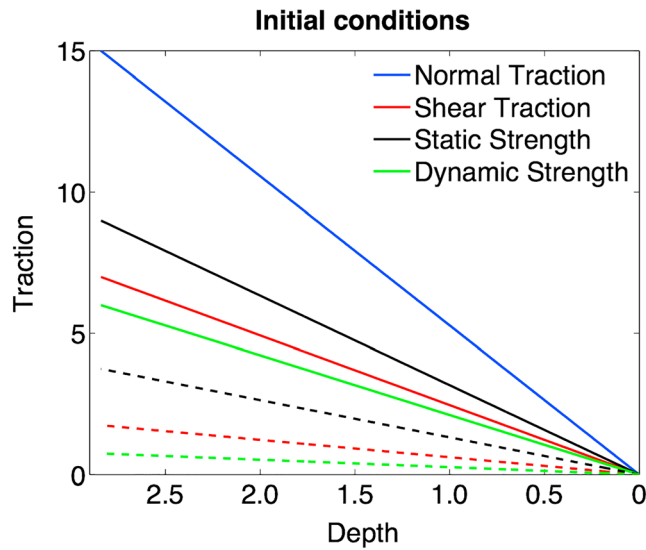


**Figure 2.** Initial traction conditions as a function of depth. Both depth and traction are expressed in terms of dimensionless parameters. The blue line represents the normal traction profile that is the same for all the simulations. Red, black, and green solid lines describe the initial shear traction, the static frictional strength, and the dynamic frictional strength, respectively, for the simulations performed imposing the highest adopted friction level ( $\mu_s = 0.60$  and  $\mu_d = 0.40$ ). Red, black, and green dashed lines describe the initial shear traction, the static frictional strength, and the dynamic strength level, respectively, for the simulations performed imposing the lowest used friction level ( $\mu_s = 0.25$  and  $\mu_d = 0.05$ ).

traction, and we impose for all simulations  $\mu_s - \mu_d = 0.2$  in order to keep the same stress drop and strength excess for all the simulations.

The initial traction and interfacial strength initial distributions are illustrated Figure 2, for an initial interface strength excess  $s = 2$  and two different sets of static and dynamic friction levels:  $\mu_s = 0.60$  and  $\mu_d = 0.40$ , and  $\mu_s = 0.25$  and  $\mu_d = 0$ . For a strength excess parameter  $s = 2$  an infinite symmetric rupture is not expected to accelerate at supershear speeds (Burrige, 1973).

The rupture is initiated by imposing the initial tangential traction slightly above the frictional strength over a finite length  $L_c$ , large enough to ensure the dynamic propagation of the rupture away from the nucleation (Scala et al., 2017; Uenishi & Rice, 2003).

Different nucleation depths were investigated (see Figure 1). Indeed, depending on the nucleation depth, the interaction can be triggered when the rupture is still in its acceleration phase or it has already reached the asymptotic speed. This aspect may control the acceleration and stationary propagation of the crack. Moreover, the memory effects inherited from the history of the radiation might play a role in controlling the rupture dynamics affecting the total stored energy in the hanging wall.

For a fixed nucleation depth, the ratio  $T_{Nuc}^t/T^n$ , with  $T_{Nuc}^t$  the tangential traction in the nucleation patch, is rescaled in order to keep constant the strength drop in the nucleation area when changing the friction coefficients.

### 3. Results

#### 3.1. Rupture Dynamics and Free Surface Wave Interaction

We examine here the implication of the symmetry breaking due to the fault-wave interaction, on the rupture dynamics as the rupture propagates along the interface toward the free surface.

In Figure 3 we show the evolution of the slip rate (blue solid lines) and the normal traction perturbation (blue dashed lines). These curves are compared with the same quantities for the case where the interface is embedded in an unbounded medium under the same initial conditions (red curves). At the same time steps we also represent the kinetic energy density field in the medium for the simulations with free surface. In Figure 4, we show the absolute values of the first invariant (volumetric deformation) and second invariant (shear deviatoric deformation) of strain tensor at the same time steps as in Figure 3.

At the early stage of the rupture ( $\tilde{t} = 2.3$ ) before the onset of the interaction, the slip rate profiles are overlapped (Figure 3a) and the waves emitted from the rupture have not yet reached the fault after being reflected/converted at the free surface. The normal traction perturbation at this stage is 0, and the solutions are the same as the ones retrieved for the symmetric rupture propagating along a planar interface embedded in an infinite medium. The symmetry across the interface is also confirmed investigating the kinetic energy field (Figure 3b) and the deformation fields (Figures 4a and 4b) at the same time.

Figure 3c shows the slip rate and the normal traction perturbation just after the onset of the interaction ( $\tilde{t} = 4.6$ ). When the interaction starts, the rupture dynamics is affected at the crack front and behind the tip where the crack is sliding at the dynamic friction level. At this time, in the upward direction, the slip rate is enhanced at the crack front. Behind the process zone, the rupture undergoes an overshoot with a further increase of the slip rate. At this stage the maximum of the normal traction perturbation is behind the process zone. This implies that the largest slip rate enhancement with respect to the unbounded case is observed in the region slipping at the dynamic friction level.

The blue dashed line in Figure 3c evidences how the increase of slip rate is due to the symmetry breaking generated by the normal traction perturbation. Ahead of the crack front, wave interaction with the

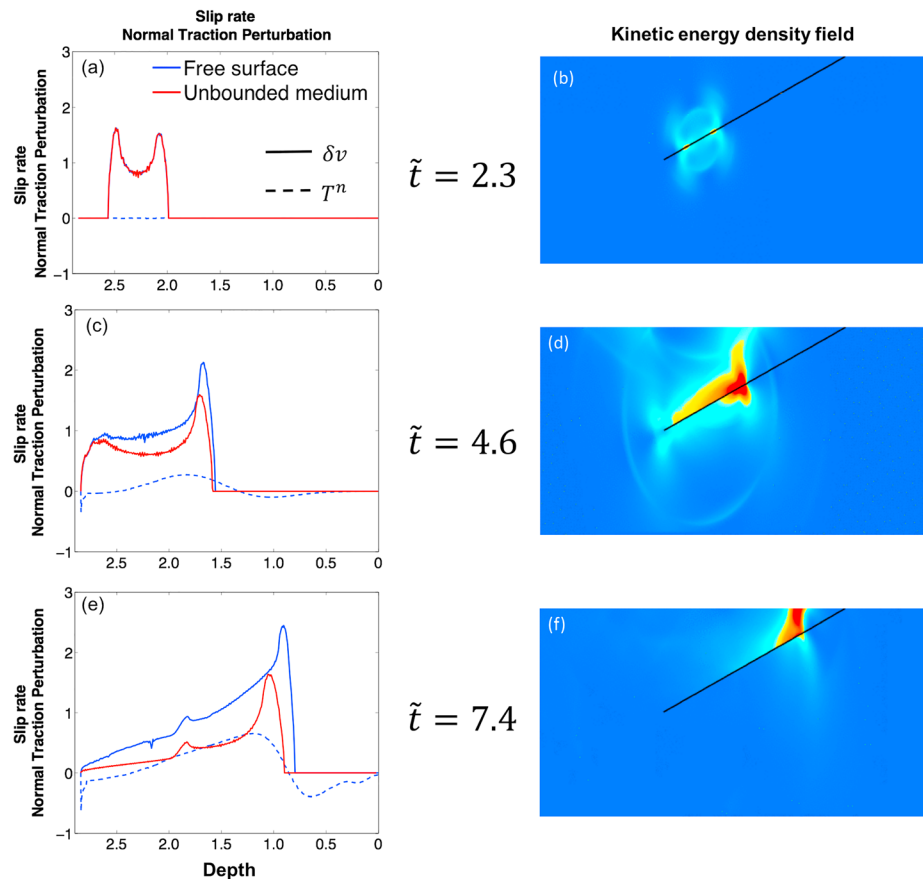


**Figure 3.** (a, c, e) The dimensionless slip rate (solid lines) and the normal traction perturbations (dashed lines) are plotted as a function of the normalized depth at the three time steps  $\tilde{t} = 2.3; 4.6; 7.4$ . The slip rate for the same simulation in an unbounded medium is plotted with a solid red curve (for the symmetric case the normal traction perturbation is 0). (b, d, f) At the same time steps, the kinetic energy density field in the medium for the free surface simulation.

unslipping part of the interface produces a compression in the normal traction. Instead, at and behind the crack front, the slip-induced normal traction perturbation is tensile, making the upward propagation favored with respect to the symmetric case as supported from laboratory (Brune, 1996) and numerical models (Nielsen, 1998; Oglesby et al., 1998, 2000).

Wave interaction of the rupture with the free surface is also shown through the kinetic energy density (Figure 3d) and the deformation fields (Figures 4c and 4d). These quantities evidence the symmetry breaking in terms of nonuniform and increasing hanging-wall stored energy due to the reflected body and surface waves produced during the rupture propagation (Brune, 1996; Shi et al., 1998). This in turn leads to a memory effect and to an increasing effective compliance of the hanging wall. As such, the effect of breaking the reflection symmetry in this system resembles that of a bimaterial rupture advancing in the direction of the slip in a more compliant medium (Andrews & Ben-Zion, 1997; Harris & Day, 1997; Rubín & Ampuero, 2007; Scala et al., 2017).

As the rupture continues to propagate upward the symmetry breaking is strengthened. As a result, the slip rate and the normal traction perturbation increase more and more. At  $\tilde{t} = 7.4$  the maximum of the slip rate at the crack front is more than twice larger than the corresponding value in an unbounded medium; the same effect is observed for the dynamic overshoot behind the process zone. In other words, when the rupture enters in the zone where the frictional strength and the stress drop are small enough to be comparable with the imposed level of cohesion, the rupture dynamics is dominated by the rupture-surface waves interaction and by the symmetry breaking. At this stage, most of the kinetic energy is concentrated in a narrow domain

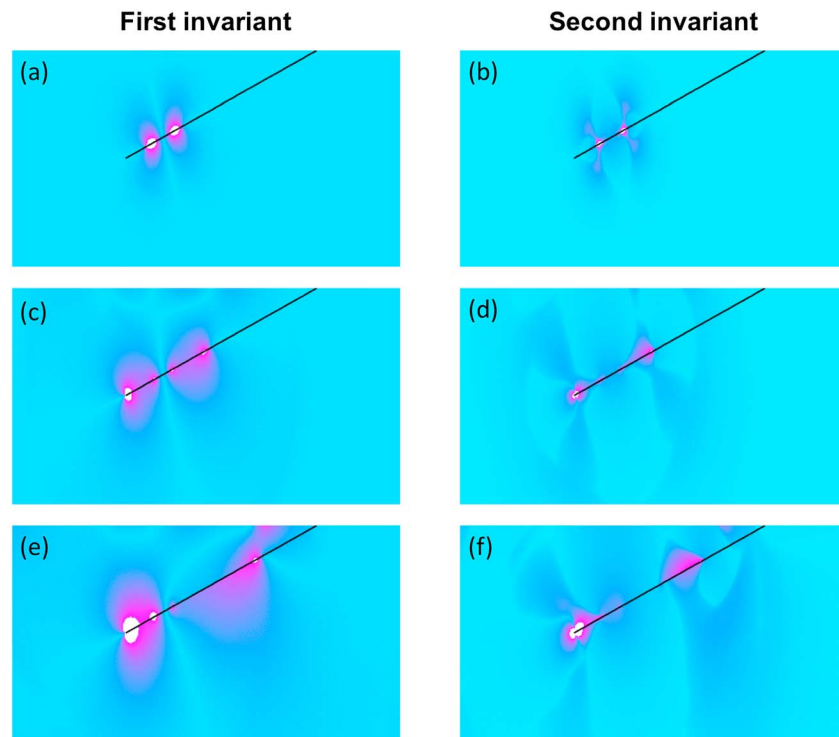


**Figure 4.** For the same time steps as in Figure 3 the absolute value of the (a, c, e) first and (b, d, f) second invariants of the strain tensor are shown, which describe the volumetric and deviatoric deformations of the medium, respectively. An evident symmetry breaking can be recognized in the snapshots (Figures 4c–4f).

around the crack front (Figure 3f). In the vicinity of the surface, most of the energy from surface and body waves is stored in the hanging wall as emerging from the deformation field in the medium (Figures 4e and 4f). This asymmetry is retrieved in the ground motion as supported by Nielsen (1998) and Oglesby et al. (2000).

To verify that the results are not affected by a mesh-related artifact, a mesh refinement analysis has been performed. The same rupture dynamics has been simulated using a refined mesh with half of the mesh size. In Figure S2 of the supporting information the slip rate curves at different stages of the dynamic rupture obtained with different mesh resolutions do superimpose, which warrants the numerical convergence of the simulations.

### 3.2. Rupture Speed and Inertial Effect

The position of the crack tip in presence of a free surface (Figure 3e) in comparison with a crack propagating in an unbounded medium indicates that the free surface-rupture wave interaction also has an effect on the rupture acceleration and thus on the average rupture speed during the upward propagation.

Figure 5a shows the time of the slip activation along the interface, during the upward propagation, as a function of the dimensionless depth  $\bar{z}$  both for the case with free surface (blue dots) and for the unbounded medium (red dots), for the same simulations as in Figure 3. After the nucleation phase, the rupture speed is the same for the two cases, as long as the interaction is not triggered. When the interaction starts, the symmetry breaking causes a faster acceleration of the rupture. Finally, both ruptures accelerate toward the Rayleigh wave speed expected as the asymptotic subshear limit for a rupture propagating in a homogenous medium (Burridge, 1973).

In this simulation the interaction is triggered when the rupture speed is at  $\sim 60\%$  of the  $S$  wave velocity. Then the increasing symmetry breaking generates a sizeable acceleration effect. The rupture accelerates

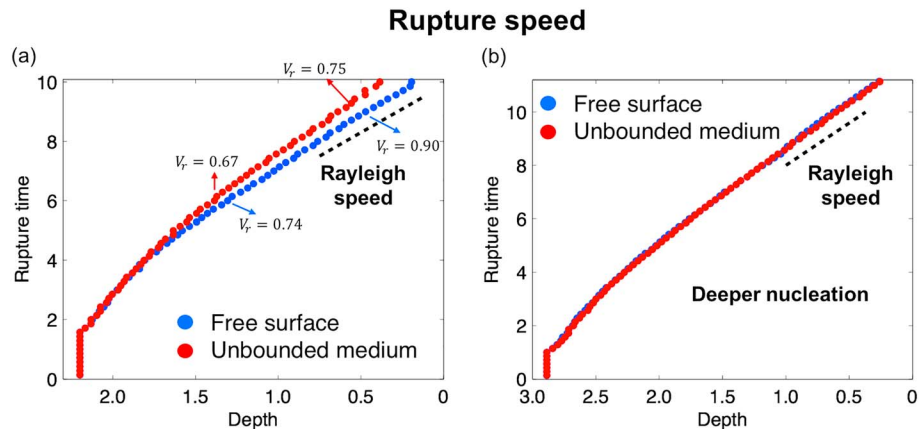


**Figure 5.** Plots of rupture time as a function of depth. (a) The rupture time is shown for the free surface (blue dots) and unbounded medium (red dots) simulations as in Figure 3. The black dashed line represents the slope corresponding to the Rayleigh speed in the medium. Both ruptures reach the asymptotic speed but at different times, as an effect of the inertia acquired by the rupture, when interacting with waves from the free surface. (b) The same quantities are plotted for a simulation having a deeper nucleation. When the asymptotic speed is reached before the wave-rupture interaction starts, the inertial effect can be neglected.

(Figure 5a) toward the asymptotic speed limit much faster in the asymmetric system than in the symmetric one.

The rupture speed, when reflection symmetry is broken, is  $\sim 10\%$  larger at a normalized depth of  $\sim 1.2$  and  $20\%$  larger in the vicinity of the surface as compared to that in the symmetric case. The values of the rupture velocity are reported in the Figure 5a.

On the contrary, if the interaction starts when the rupture is close to the Rayleigh speed, both the symmetric and asymmetric ruptures proceed at the same numerical speed limit. This is illustrated in Figure 5b, for a numerical simulation realized with the same geometrical and initial conditions but with a deeper nucleation.

When the rupture approaches the asymptotic speed limit, the energy spent to further accelerate the rupture tends to 0, and the stored energy in the hanging wall increases the effects of the symmetry breaking. This leads to a more pronounced increase of the maximum slip rate at the crack front and of the maximum of tensile normal traction perturbation as shown in Figure S3 in the supporting information.

This nonclassical rupture acceleration effect is a complex effect triggered by two coupled factors: First, the slip-induced tensile normal traction perturbation at and behind the crack tip leads to a weakening of the interface that promotes the upward rupture acceleration toward the asymptotic speed limit; second, effective inertial dynamics is inherited from wave interaction of the rupture with the free surface during the upward propagation giving rise to memory and effective hanging-wall mass.

The latter factor is supported by theoretical results (Fineberg & Bouchbinder, 2015; Marder, 1991) in the case of a crack propagating in an externally loaded infinite strip. Even if the system possesses a reflection symmetry, wave interaction of the rupture with boundaries leads to an energy release rate involving an inertial term and an effective mass, which decreases to 0 as the rupture speed approaches the speed limit. Experimental results are also supporting these theoretical results evidencing a sluggish acceleration of the rupture in a strip, toward a speed limit lower than the Rayleigh wave speed. Conversely, we have shown that the symmetry breaking in the case of dipping reverse faults always favors the rupture acceleration toward the limit speed, owing to the slip-induced tensile normal stress perturbation behind the crack tip.

### 3.3. Friction-Level Sensitivity

For symmetric ruptures in unbounded elastic media, the energy balance is controlled by the frictional strength and the stress drop all along the rupture propagation and therefore by the strength excess  $s$ . The friction level does not modify the rupture dynamics as far as it does not affect these parameters.

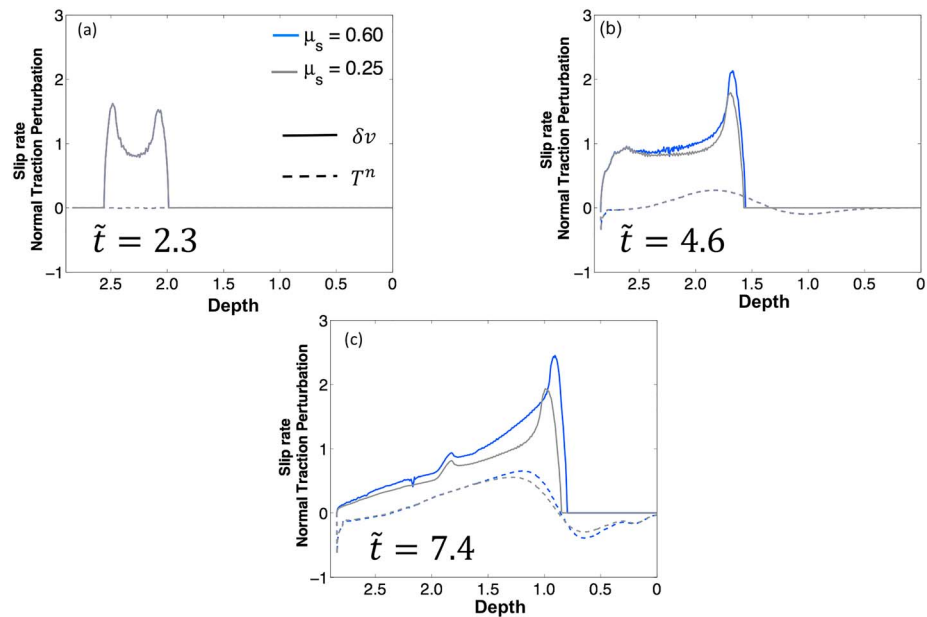


**Figure 6.** Comparison between simulations with different friction levels. The slip rate (solid lines) and the normal traction perturbation (dashed lines) are plotted as a function of the normalized depth for two levels of friction at the same time steps as in Figure 3. The blue curves are obtained for  $\mu_s = 0.60$  and  $\mu_d = 0.40$ , and the gray curves for  $\mu_s = 0.25$  and  $\mu_d = 0.05$ .

Recent theoretical analysis has shown that when the reflection symmetry across the interface is broken by the effect of wave interaction of the rupture with boundary, the linear stability condition governing the unstable dynamic propagation includes an explicit dependence on the friction level (Aldam et al., 2016).

The slip rate and normal interface traction perturbation are shown in Figure 6 for two numerical experiments performed with different sets of friction coefficients ( $\mu_s = 0.60$  and  $\mu_d = 0.40$ , and  $\mu_s = 0.25$  and  $\mu_d = 0.05$ ), at the same time steps as in Figure 3.

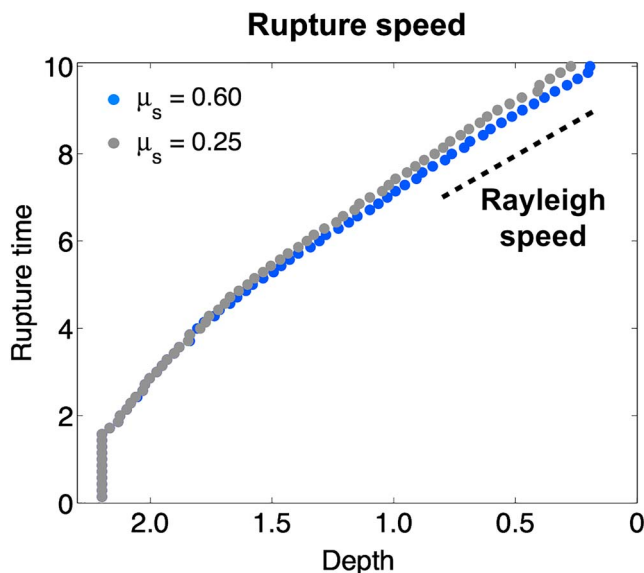


**Figure 7.** Rupture time as a function of normalized depth for the two simulations with  $\mu_s = 0.60$  and  $\mu_d = 0.40$  (blue dots) and  $\mu_s = 0.25$  and  $\mu_d = 0.05$  (gray dots).

At time  $\tilde{t} = 2.3$  (Figure 6a) wave interaction of the rupture with the free surface has not yet been triggered, and the two solutions are identical and independent of the absolute level of friction.

After the triggering ( $\tilde{t} = 4.6$ ; Figure 6b) the increase of the slip rate at and behind the crack front is larger for the largest level of the friction. At this stage, both systems undergo a breaking of the reflection symmetry, which is evidenced by a tensile slip-induced normal traction perturbation behind the crack front, which is still undistinguishable between the two simulations.

At a later time ( $\tilde{t} = 7.4$ ), the difference between the two systems in term of the maximum slip rate at the crack front increases more and more. This is driven by the difference in amplitude of the slip-induced normal traction perturbation in the two cases (Figure 6c). When the reflection symmetry is broken, the traction perturbation is triggered, and the coupling of the tangential slip with the normal traction increases with the level of friction.

The absolute level of friction is also affecting the rupture acceleration. The larger the friction level, the faster the acceleration is toward the Rayleigh speed (Figure 7). This is, to our knowledge, a new result with important implications for reverse-fault rupture dynamics.

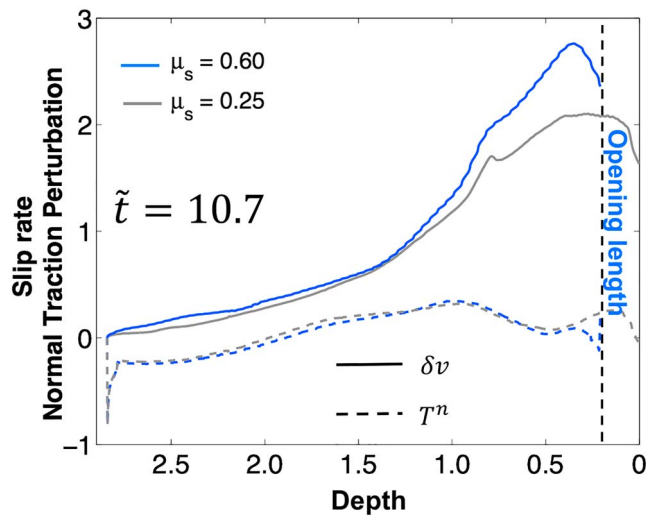


**Figure 8.** Slip rate (solid lines) and normal traction perturbation (dashed lines) plotted as a function of depth for  $\mu_s = 0.60$  and  $\mu_d = 0.40$  (blue dots) and for  $\mu_s = 0.25$  and  $\mu_d = 0.05$  (gray dots). The black vertical dashed line marks the opening domain for the simulation with  $\mu_s = 0.60$ .

traction is negative) and the opened part of the interface (where the total normal traction is 0) is marked in Figure 8 by a black dashed line. At this point the asymmetric deformation around the propagating crack front is instantaneously released as an effect of the end of the frictional propagation (Figure S4 in the supporting information).

For a system that possesses reflection symmetry (unbounded system) we never observe an opening of the interface, even if the topmost point of the interface has zero normal traction to mimic the same initial conditions.

The intensity of the slip-induced normal traction perturbation effect depends on the friction. In Figure 8, at  $\tilde{t} = 10.7$ , the solid and dashed gray curves represent the slip rate and the normal traction perturbation for the smallest friction level. In this case, no opening occurs, and frictional slip may propagate up to the free surface.

For the same initial traction conditions, the opening effect is controlled by both the nucleation depth and the friction level. Figure 9a shows the opening length as a function of the barycenter of the nucleation patch. The deeper the nucleation, the larger the opening length is. Since a larger opening domain implies a stronger induced normal traction perturbation, this effect is due to the larger amount of radiation emitted by the rupture and stored in the hanging wall. Similar results are obtained as a function of the static level of friction: The larger the friction values, the longer the opening patch is (Figure 9b).

### 3.5. Shallow Slip and Surface Displacement

In all simulations, strong and asymmetric ground motion and surface deformation are the signature of an asymmetric distribution of the kinetic and of the history-dependent stored energy that results from the geometric broken reflection symmetry across the interface as the rupture propagates upward. This is supported by previous numerical results (e.g., Nielsen, 1998; Oglesby et al., 2000).

Figure 10a shows the coseismic slip distribution, as a function of the depth, along the interface for two different cases with the same dipping-interface geometry and nucleation depth, but with different absolute level of friction, for example, ( $\mu_s = 0.6$  and  $\mu_d = 0.4$ ) and ( $\mu_s = 0.25$  and  $\mu_d = 0.05$ ). For comparison, a result for the latter friction condition but in a system that possesses reflection symmetry (unbounded medium) is also added.

While for asymmetric system the maximum interface slip is concentrated around the nucleation zone, the symmetry breaking leads to large amplitude slip that increases along the upward portion of the interface

### 3.4. Interface Opening

In the previous subsections we have shown how reflection symmetry breaking, due to wave interaction of the rupture with the free surface, leads to a tensile slip-induced normal traction perturbation at and behind the crack front.

As the rupture propagates updip, the tensile slip-induced traction perturbation occurs in regions of the fault where the initial normal traction is smaller and smaller. Thus, in the vicinity of the free surface, the initial normal traction becomes small enough to possibly allow an opening of the interface.

Figure 8 shows, at the dimensionless time step  $\tilde{t} = 10.7$ , the distributions of the slip rate and normal traction perturbation for the two simulations described in the previous subsection.

For the largest friction level (blue curves), an opening of the interface starts at the crack tip and then, almost instantaneously, propagates toward the surface, through the portion of the interface where a compressive perturbation was previously induced by the waves. This portion has a finite length, and after the opening, it no longer comes back in contact, behaving as a free surface. The separation between the frictionally sliding portion of the interface (where a slip rate is defined and the total normal

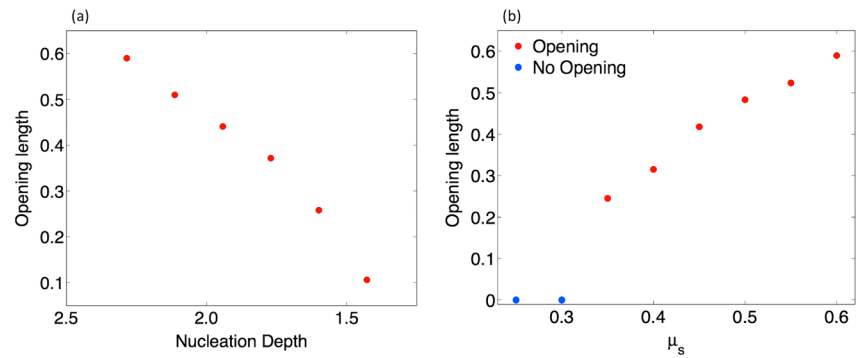


**Figure 9.** (a) The opening length is plotted as a function of the nucleation depth. (b) The opening length is plotted as a function of the static friction coefficient. The blue dots indicate that for small friction values the opening does not occur. The opening length increases with both nucleation depth and friction level.

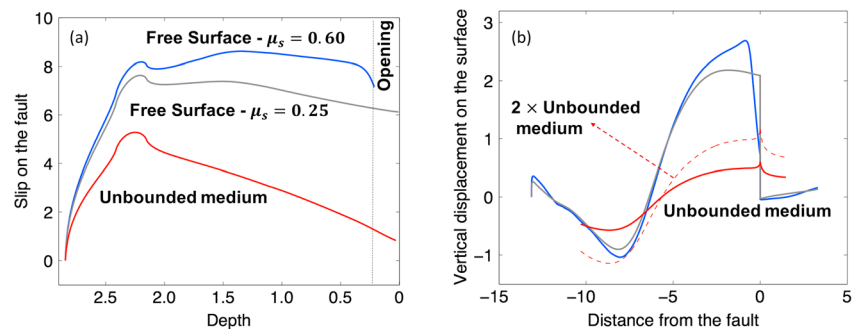
and reaches a kind of plateau, for both sets of friction. The higher the friction, the larger is the maximum slip amplitude. Slip in the vicinity of the free surface is generally about 3 to 4 times larger than that in the unbounded case.

Figure 10b shows the static vertical displacement along the free surface, as a function of the horizon distance measured from the intersection of the frictional interface with the free surface. Strong uplift on the hanging-wall side, close to the interface, is the signature of geometric reflection asymmetry as a result of the wave interaction history of the rupture with the free surface. As such, the static vertical displacement depends also on the absolute level of friction of the interface.

### 3.6. Interface Cohesion

In this model, small stress perturbations driven by waves may induce episodic unrealistic sliding near the free surface disconnected from the mother crack, since the frictional strength goes to 0 in the upper portion of the interface. The use of a small, though nonzero cohesion helps in limiting this effect.

To evaluate the influence of the interface cohesion, we compare the solutions obtained in the previous sections with simulations where  $C = 0$ . In Figure 11 we compare the slip rate and the normal traction perturbation for the same system as in Figure 3 at two different time steps during the rupture propagation. The different energy balance, due to the lack of the cohesion, leads to an enhanced updip propagation in terms of both maximum of slip rate at the crack front and rupture velocity (black curves).



**Figure 10.** (a) The final slip on the fault is plotted as a function of depth for an unbounded simulation (red curve), a free surface simulation with the lowest level of friction (gray curve), and a free surface simulation with the highest level of friction (blue curve). The vertical dashed line marks the opening domain for this latter simulation. (b) For the same simulations, the static vertical distance is plotted as a function of the horizontal distance from the point of the fault on the surface. Negative values represent points on the hanging wall (see Figure 1), while positive ones refer to points on the footwall. The red dashed line is the result of the solid line multiplied by 2, this factor accounting at the first order for the free surface effect.

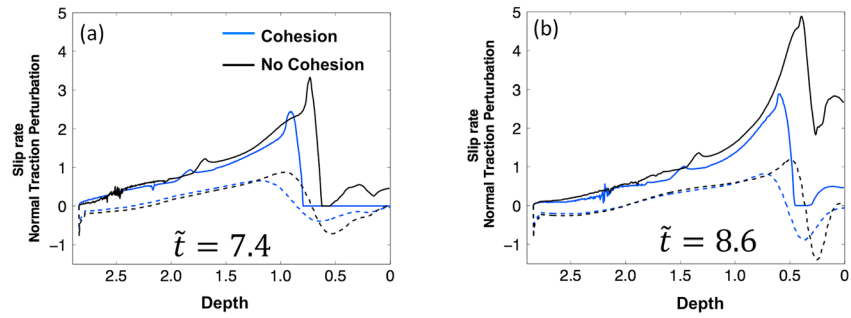


**Figure 11.** Comparison between two simulations for which  $C \neq 0$  (blue curves) and  $C = 0$  (black curves). The dimensionless time (a)  $\tilde{t} = 7.4$  and (b)  $\tilde{t} = 8.6$ . Solid and dashed lines show the spatial distribution of the slip rate and the normal traction perturbation, respectively.

When there is no interface cohesion, a secondary crack emerges ahead of the rupture front, increasing the compressive perturbation ahead the mother rupture front associated with seismic waves. The secondary crack propagates up to the free surface, while it is initially suppressed by the use of a cohesion (Figure 11a) and emerges later close to the surface (Figure 11b).

It is worthy to note that despite the fact that the different energy balance slightly changes the rupture dynamics between the two cases, the cohesion does not change the qualitative behavior of the rupture dynamics, the rupture-wave interaction, the changes in the rupture speed, and the interface opening features.

In the case where  $C \neq 0$ , when the normal traction goes to 0 (opening condition), an instantaneous stress drop by an amount of  $C$  occurs, transferring elastodynamic energy around the opened portion of the interface. However, due to the low cohesion level, this energy is negligible compared to the energy stored in the hanging wall and no significant dynamic effect emerges. Moreover, this stress drop does not trigger spurious effect on the results as shown by the grid refinement analysis.

#### 4. Discussion and Conclusions

In this work, combining different numerical experiments, we deeply investigated how the dynamics of a thrust rupture reaching the surface is controlled by the symmetry breaking due to the interaction of the fault interface with the seismic waves in the vicinity of the free surface.

Seismic waves radiated during the rupture propagation get reflected/converted at the free surface and trigger a rupture/surface interaction when they reach the crack again. As such the crack is interacting with its own history giving rise to memory. Using simple geometrical considerations, the distance  $d_i$  from the free surface at which this interaction affects the crack tip depends on the nucleation depth  $d_n$ , the dip angle  $\theta$ , the  $S$  wave velocity  $V_s$ , and the average rupture speed  $\hat{V}_r$ , according to the formula:

$$d_i = d_n \left( 1 - \frac{\hat{V}_r \cdot \sin\theta}{\sqrt{V_s^2 - \hat{V}_r^2 \cdot \cos^2\theta}} \right) \quad (4)$$

This quantity is normalized by a characteristic length scale of the problem that is expressed in equation (4) by the nucleation depth; the faster the rupture, the shallower the trigger of the interaction. More details about this geometrical interpretation are provided in the supporting information (see Figure S5 and the related text).

We finely investigated how this wave interaction controls the coupling between the shear and the normal traction perturbation, which is shown to be compressive ahead of the crack front and extensional behind it. Signature of this geometric breaking of the reflection symmetry can be found on the radiated energy and the history-dependent stored energy in the hanging wall. As a result, the surface ground motion is also asymmetric as also evidenced by previous numerical and laboratory studies (Nielsen, 1998; Oglesby et al.,

1998, 2000; Uenishi, 2015; Ma & Archuleta, 2006) and expected from seismological observations (Abrahamson & Sommerville, 1996; Vallage et al., 2015). We found that the symmetry breaking leads to an enhancement of the slip rate at the crack tip, associated with a sudden decrease of frictional strength similarly to a bimaterial interface case (Harris & Day, 1997).

We also found as a new result that the geometric asymmetry induced by the wave interaction of the rupture with the free surface drives faster acceleration of the rupture toward the asymptotic Rayleigh wave speed limit than in a symmetric configuration. This is due to the tensile normal traction perturbation and inherited inertial dynamics involving a velocity-dependent effective mass (Marder, 1991). This is in contrast with the rupture propagation within an infinite strip, where the inertia dynamics inherited from rupture/wave interaction reduces the acceleration of the rupture toward the limit speed (Fineberg & Bouchbinder, 2015; Goldman et al., 2010). It is worthy to note here that in our idealized reverse fault, the stronger acceleration does not lead to a short rupture time. Indeed, the rupture does not arrest when it impacts against the free surface because the surface waves trapped in the hanging wall continue to sustain the slip growth with time leading to average longer rupture durations for ruptures lacking the reflection symmetry.

An important outcome of this study is that the symmetry breaking leads to a dependence of the rupture dynamics on the absolute level of friction: A higher level of friction induces a larger amplitude of the slip-induced normal traction perturbations, which in turn favor the updip rupture propagation increasing the inertia effect and the slip rate enhancement. This result is supported by a linear stability analysis (Aldam et al., 2016) showing frictional dependence of the sliding for a system that lacks reflection symmetry across the interface.

We then found that when the rupture propagates along the shallowest portion of the interface, where the initial normal traction and stress drop decrease, the tensile traction perturbation may lead to an interface opening. This feature propagates almost instantaneously up to the free surface with the two sides of the interface separating along a finite length of the interface. We also found that the opening effect is also dependent on the frictional level and the rupture propagation distance from the nucleation, and for small values of the friction, the opening does not occur.

A recent laboratory study (Gabuchian et al., 2017) also supported the possibility of an interface opening as a result of a torque mechanism. Such torque mechanism might result from large deformations as the rupture approaches the free surface, which are not investigated in this study, where the simulations are performed under a small deformation hypothesis.

Beyond this, the opening effect of a crack reaching the free surface has been already shown in the numerical experiments by Shi et al. (1998), confirming the laboratory results by Brune (1996). However, diversely from these models the features of the opening are different. In our model, where the tectonic loading increases with depth, with small normal and tangential traction close to the surface, the opening is limited to a region close to the surface and does not propagate back along the fault. In addition, the two sides of the fault do not longer come in contact after the opening. The use of a high-resolution numerical method with nonsmooth contact and friction conditions, such as the spectral element method, allows to characterize how the opening is generated and to analyze the size of the opening region as a function of the friction coefficient and the nucleation depth.

As a direct implication of this study, we showed that in our model the effect of wave interaction of the rupture with the free surface drives strong amplification and asymmetry of shallow slip and large vertical static surface displacement, which have important implications in terms of tsunami source and tsunami potential for an off-shore event. Recent studies have shown that a large amount of slip from several thrust earthquakes concentrates along the shallower part of the fault both at large collision zones (e.g., in the case of the 1999  $M_w$ 7.7 Chi-Chi earthquake; Tanaka et al., 2006; Zhang et al., 2008) and along subduction interfaces, such as for the 2004  $M_w$  9.2 Sumatra earthquake and the 2011  $M_w$  9.1 Tohoku earthquake (Lay, 2018; Lorito et al., 2016; Romano et al., 2014; Shearer & Bürgmann, 2010). The unexpectedly large slip in the shallow low-rigidity portion of the subducting plate was identified as responsible for the huge tsunami waves that devastated the near coastal areas (e.g., Mori et al., 2011; Satake et al., 2013). Moreover, the longer average rupture duration is a feature commonly observed for shallow earthquakes (Bilek & Lay, 1999; Geist & Bilek, 2001) as well as for the so-called tsunami earthquakes such as the historical 1896  $M_s$  7.2 Sanriku

(Tanioka & Satake, 1996) and 2010  $M_w$  7.8 Mentawai earthquakes (Yue et al., 2015). In our results, all these effects are shown to be dependent on the level of friction, and they are always significant when compared to the symmetric case.

Broken reflection symmetry in reverse-fault systems can also be constitutive in nature, and more realistic reverse-fault models could include softer shallow layers, such as accretionary prisms in subduction zones, and inelastic dissipative mechanisms in the hanging wall (e.g., Ma & Beroza, 2008; Ma, 2012; Ma & Hirakawa, 2013; Kozdon & Dunham, 2013; Lotto et al, 2017). When rupture enters or interacts with such layers, the absolute value of the rupture speed might decrease even for a constant ratio between the rupture speed and the  $S$  wave speed (Murphy et al., 2018). Constitutive bimaterial might enhance the effect of the wave interaction of the rupture with the free surface and increase the coupling between interfacial slip and normal traction perturbation (e.g., Ma & Beroza, 2008). This can contribute to increasing the rupture duration in the case of shallow events. Moreover, small friction levels in the vicinity of shallow accretionary sediments might affect the amplification of the vertical ground motion (Murphy et al., 2018). Inelastic dissipation effects in the hanging wall, such as off-fault damage or plasticity (Thomas & Bhat, 2018), may also contribute in the ground motion damping.

We selected a single dip angle for our simulation ( $20^\circ$ ) that corresponds to an intermediate value for some subducting interfaces, between the very low dip angles in the vicinity of the oceanic trenches (Kozdon & Dunham, 2013) and the steepest slopes revealed by seismic imaging at larger depths (Satriano et al., 2014; Takahashi et al., 2004). A more extended parametric study might allow us to assess more quantitatively the wave interaction effect of the rupture with the free surface, as a function, for example, of the dip angle and of the initial traction profile along the interface. Nevertheless, as long as the hypothesis of increasing initial normal traction with depth can be considered valid, the interpretation framework provided in this study can be at least qualitatively extended to interfaces with smaller dip angles.

Finally, since no system is perfectly symmetric, we believe that geometrically induced coupling between interfacial slip and normal traction perturbation, induced by wave interaction of the rupture with boundaries, may exist in a broad range of frictional fault systems. Consequently, coupling of seismic waves with the rupture should be incorporated in various numerical approaches and when interpreting geophysical observations.

#### Acknowledgments

The data for this paper can be accessed at the doi: <https://doi.org/10.6084/m9.figshare.6940805>. The authors would like to thank Harsha Bhat and Raul Madariaga for fruitful scientific discussion during this work. The numerical simulations were performed on the High-Performance Computing Auriga cluster at INGV, with the support of Daniele Melini, and on the High-Performance Computing and Data Analysis platform (S-CAPAD) at IPGP, with the support of Geneviève Moguilny. The authors also acknowledge projects TSUMAPS-NEAM and SERA for supporting the activity. TSUMAPS-NEAM (<http://www.tsumaps-neam.eu/>) is an European Project co-financed by the European Union Civil Protection Mechanism, Agreement Number: ECHO/SUB/2015/718568/PREV26. SERA has received funding from the European Union's HORIZON 2020 with the project ID 730900.

#### References

- Abrahamson, N. A., & Sommerville, P. G. (1996). Effects of the hanging-wall and footwall on ground motions recorded during the Northridge earthquake. *Bulletin of Seismological Society of America*, *86*(1B), S93–S99.
- Aldam, M., Bar-Sinai, Y., Svetlizky, I., Brener, E. A., Fineberg, J., & Bouchbinder, E. (2016). Frictional sliding without geometrical reflection symmetry. *Physical Review*, *6*, 041023. <https://doi.org/10.1103/PhysRevX.6.041023>
- Andrews, D. J., & Ben-Zion, Y. (1997). Wrinkle-like slip pulse on a fault between different materials. *Journal of Geophysical Research*, *102*, 553–571. <https://doi.org/10.1029/96JB02856>
- Bilek, S. L., & Lay, T. (1999). Rigidity variations with depth along interplate megathrust faults in subduction zones. *Nature*, *400*(6743), 443–446. <https://doi.org/10.1038/22739>
- Brener, E. A., Weikamp, M., Spatschek, R., Bar-Sinai, Y., & Bouchbinder, E. (2016). Dynamic instabilities of frictional sliding at a bimaterial interface. *Journal of the Mechanics and Physics of Solids*, *89*, 149–173. <https://doi.org/10.1016/j.jmps.2016.01.009>
- Brune, J. N. (1996). Particle Motions in a Physical Model of Shallow Angle Thrust Faulting. *Proceedings of the Indian Academy of Sciences – Earth and Planetary Science*, *105*(2), L197–L206.
- Burridge, R. (1973). Admissible speeds for plane-strain self-similar shear cracks with friction but lacking cohesion. *Geophysical Journal International*, *35*(4), 439–455. <https://doi.org/10.1111/j.1365-246X.1973.tb00608.x>
- Erdogan, F., & Arin, K. (1975). Half plane and a slip with an arbitrary located crack. *International Journal of Fracture*, *11*(2), 191–204. <https://doi.org/10.1007/BF00038888>
- Festa, G., Delavaud, E., & Vilotte, J.-P. (2005). Interaction between surface waves and absorbing boundaries for wave propagation in geological basins: 2D numerical simulations. *Geophysical Research Letters*, *32*, L20306. <https://doi.org/10.1029/2005GL024091>
- Festa, G., & Vilotte, J.-P. (2005). The Newmark scheme as velocity-stress time-staggering: An efficient implementation for spectral element simulations of Elastodynamics. *Geophysical Journal International*, *161*(3), 789–812. <https://doi.org/10.1111/j.1365-246X.2005.02601.x>
- Festa, G., & Vilotte, J.-P. (2006). Influence of rupture initiation on the intersonic transition: Crack-like versus pulse-like modes. *Geophysical Research Letters*, *33*, L15320. <https://doi.org/10.1029/2006GL026378>
- Fineberg, J., & Bouchbinder, E. (2015). Recent developments in dynamic fracture: Some perspectives. *International Journal of Fracture*, *196*(1–2), 33–57. <https://doi.org/10.1007/s10704-015-0038-x>, arXiv 1504.04851
- Gabuchian, V., Rosakis, A. J., Bhat, H. S., Madariaga, R., & Kanamori, H. (2017). Experimental evidence that thrust earthquake ruptures might open faults. *Nature*, *545*(7654), 336–339. <https://doi.org/10.1038/nature22045>
- Gabuchian, V., Rosakis, A. J., Lapusta, N., & Oglesby, D. D. (2014). Experimental investigation of strong ground motion due to thrust fault earthquakes. *Journal of Geophysical Research: Solid Earth*, *119*, 1316–1336. <https://doi.org/10.1002/2013JB010409>
- Geist, E. L., & Bilek, S. L. (2001). Effect of depth-dependent shear modulus on tsunami generation along subduction zones. *Geophysical Research Letters*, *28*, 1315–1318. <https://doi.org/10.1029/2000GL012385>

- Goldman, T., Livne, A., & Fineberg, J. (2010). Acquisition of inertia by a moving crack. *Physical Review Letters*, *104*, 114301. <https://doi.org/10.1103/PhysRevLett.104.114301>
- Harris, R. A., & Day, S. M. (1997). Effects of a low-velocity zone on a dynamic rupture. *Bulletin of Seismological Society of America*, *87*, 1267–1280.
- Huang, Y., Meng, L., & Ampuero, J.-P. (2012). A dynamic model of the frequency-dependent rupture process of the 2011 Tohoku-Oki earthquake. *Earth, Planets and Space*, *64*(12), 1061–1066. <https://doi.org/10.5047/eps.2012.05.011>
- Ida, Y. (1972). Cohesive force across the tip of a longitudinal-shear crack and Griffith's specific surface energy. *Journal of Geophysical Research*, *77*, 3796–3805. <https://doi.org/10.1029/JB077i020p03796>
- Komatitsch, D., & Vilotte, J.-P. (1998). The spectral element method: An efficient tool to simulate the seismic response of 2D and 3D geological structures. *Bulletin of Seismological Society of America*, *88*, 368–392.
- Kozdon, J. E., & Dunham, E. M. (2013). Rupture to the trench: Dynamic rupture simulations of the 11 March 2011 Tohoku earthquake. *Bulletin of the Seismological Society of America*, *103*(2B), 1275–1289. <https://doi.org/10.1785/0120120136>
- Lay, T. (2018). A review of the rupture characteristics of the 2011 Tohoku-oki Mw 9.1 earthquake. *Tectonophysics*, *733*, 4–36. <https://doi.org/10.1016/j.tecto.2017.09.022>
- Lorito, S., Romano, F., & Lay, T. (2016). Tsunamigenic major and great earthquakes (2004–2013): Source processes inverted from seismic, geodetic, and sea-level data. In *Springer encyclopedia of complexity and system science* (pp. 1–52). New York: Springer Science + Business Media. [https://doi.org/10.1007/978-3-642-27737-5\\_641-1](https://doi.org/10.1007/978-3-642-27737-5_641-1)
- Lotto, G. C., Dunham, E. M., Jeppson, T. N., & Tobin, H. J. (2017). The effect of compliant prisms on subduction zone earthquakes and tsunamis. *Earth and Planetary Science Letters*, *458*, 213–222. <https://doi.org/10.1016/j.epsl.2016.10.050>
- Ma, S. (2012). A self-consistent mechanism for slow dynamic deformation and tsunami generation for earthquakes in the shallow subduction zone. *Geophysical Research Letters*, *39*, L11310. <https://doi.org/10.1029/2012GL051854>
- Ma, S., & Archuleta, R. J. (2006). Radiated seismic energy based on dynamic rupture models of faulting. *Journal of Geophysical Research*, *111*, B05315. <https://doi.org/10.1029/2005JB004055>
- Ma, S., & Beroza, G. C. (2008). Rupture dynamics on a bimaterial interface for dipping faults. *Bulletin of the Seismological Society of America*, *98*(4), 1642–1658. <https://doi.org/10.1785/0120070201>
- Ma, S., & Hirasaka, E. T. (2013). Dynamic wedge failure reveals anomalous energy radiation of shallow subduction earthquakes. *Earth and Planetary Science Letters*, *375*, 113–122. <https://doi.org/10.1016/j.epsl.2013.05.016>
- Marder, M. (1991). New dynamical equation for cracks. *Physical Review Letters*, *66*(19), 2484–2487. <https://doi.org/10.1103/PhysRevLett.66.2484>
- Mori, N., Takahashi, T., Yasuda, T., & Yanagisawa, H. (2011). Survey of 2011 Tohoku earthquake tsunami inundation and run-up. *Geophysical Research Letters*, *38*, L00G14. <https://doi.org/10.1029/2011GL049210>
- Murphy, S., Di Toro, G., Romano, R., Scala, A., Lorito, S., Spagnuolo, E., et al. (2018). Tsunamigenic earthquake simulations using experimentally derived friction laws. *Earth and Planetary Science Letters*, *486*, 155–165. <https://doi.org/10.1016/j.epsl.2018.01.011>
- Murphy, S., Scala, A., Herrero, A., Lorito, S., Festa, G., Trasatti, E., et al. (2016). Shallow slip amplification and enhanced tsunami hazard unravelled by dynamic simulations of mega-thrust earthquakes. *Scientific Reports*, *6*, 35007. <https://doi.org/10.1038/srep35007>
- Nielsen, S. B. (1998). Free surface effects on the propagation of dynamic rupture. *Geophysical Research Letters*, *25*, 125–128. <https://doi.org/10.1029/97GL03445>
- Oglesby, D. D., Archuleta, R. J., & Nielsen, S. B. (1998). Earthquakes on dipping faults: The effects of broken symmetry. *Science*, *280*(5366), 1055–1059. <https://doi.org/10.1126/science.280.5366.1055>
- Oglesby, D. D., Archuleta, R. J., & Nielsen, S. B. (2000). Dynamics of dip-slip faulting: Explorations in two dimensions. *Journal of Geophysical Research*, *105*, 13,643–13,653. <https://doi.org/10.1029/2000JB900055>
- Romano, F., Trasatti, E., Lorito, S., Pìromallo, C., Piatanesi, A., Ito, Y., et al. (2014). Structural control on the Tohoku earthquake rupture process investigated by 3D FEM, tsunami and geodetic data. *Scientific Reports*, *4*(1), 5631. <https://doi.org/10.1038/srep05631>
- Rubin, A. M., & Ampuero, J.-P. (2007). Aftershock asymmetry on a bimaterial interface. *Journal of Geophysical Research*, *112*, B05307. <https://doi.org/10.1029/2006JB004337>
- Rudnicki, J. W., & Wu, M. (1995). Mechanics of dip-slip faulting in an elastic half-space. *Journal of Geophysical Research*, *100*, 22,173–22,186. <https://doi.org/10.1029/95JB02246>
- Satake, K., Fujii, Y., Harada, T., & Namegaya, Y. (2013). Time and space distribution of coseismic slip of the 2011 Tohoku earthquake as inferred from tsunami waveform data. *Bulletin of the Seismological Society of America*, *103*(2B), 1473–1492. <https://doi.org/10.1785/0120120122>
- Satriano, C., Dionicio, V., Miyake, H., Uchida, N., Vilotte, J.-P., & Bernard, P. (2014). Structural and thermal control of seismic activity and megathrust rupture dynamics in subduction zones: Lessons from the Mw 9.0, 2011 Tohoku earthquake. *Earth and Planetary Science Letters*, *403*, 287–298. <https://doi.org/10.1016/j.epsl.2014.06.037>
- Scala, A., Festa, G., & Vilotte, J.-P. (2017). Rupture dynamics along bimaterial interfaces: A parametric study of the shear-normal traction coupling. *Geophysical Journal International*, *209*(1), ggw489–ggw467. <https://doi.org/10.1093/gji/ggw489>
- Shearer, P., & Bürgmann, R. (2010). Lessons learned from the 2004 Sumatra-Andaman megathrust rupture. *Annual Review of Earth and Planetary Sciences*, *38*(1), 103–131. <https://doi.org/10.1146/annurev-earth-040809-152537>
- Shi, B., Anooshehpour, A., Brune, J. N., & Zeng, Y. (1998). Dynamics of thrust faulting: 2D lattice model. *Bulletin of the Seismological Society of America*, *88*(6), 1484–1494.
- Takahashi, N., Kodaira, S., Tsuru, T., Park, J.-O., Kaneda, Y., Suyehiro, K., et al. (2004). Seismic structure and seismogenesis off Sanriku region, northeastern Japan. *Geophysical Journal International*, *159*(1), 129–145. <https://doi.org/10.1111/j.1365-246X.2004.02350.x>
- Tanaka, H., Chen, W. M., Wang, C. Y., Ma, K. F., Urata, N., Mori, J., & Ando, M. (2006). Frictional heat from faulting of the 1999 Chi-Chi, Taiwan earthquake. *Geophysical Research Letters*, *33*, L16316. <https://doi.org/10.1029/2006GL026673>
- Tanioka, Y., & Satake, K. (1996). Fault parameters of the 1896 Sanriku tsunami earthquake estimated from tsunami numerical modeling. *Geophysical Research Letters*, *23*, 1549–1552. <https://doi.org/10.1029/96GL01479>
- Thomas, M. Y., & Bhat, H. S. (2018). Dynamic evolution of off-fault medium during an earthquake: A micromechanics based model. *Geophysical Journal International*, *214*, 1267–1280. <https://doi.org/10.1093/gji/ggy129>
- Uenishi, K. (2015). Dynamic dip-slip fault rupture in a layered geological medium: Broken symmetry of seismic motion. *Engineering Failure Analysis*, *58*(2), 380–393. <https://doi.org/10.1016/j.engfailanal.2015.07.004>
- Uenishi, K., & Rice, J. R. (2003). Universal nucleation length for slip-weakening rupture instability under nonuniform fault loading. *Journal of Geophysical Research*, *108*(B1), 2042. <https://doi.org/10.1029/2001JB001681>
- Village, A., Klinger, Y., Grandin, R., Bhat, H. S., & Pierrot-Deseilligny, M. (2015). Inelastic surface deformations during the 2013  $M_w$  7.7 Balochistan, Pakistan, earthquake. *Geology*, *43*(12), 1079–1082. <https://doi.org/10.1130/G37290.1>

- Yue, H., Lay, T., Li, L., Yamazaki, Y., Cheung, K. F., Rivera, L., et al. (2015). Validation of linearity assumptions for using tsunami waveforms in joint inversion of kinematic rupture models: Application to the 2010 Mentawai Mw 7.8 tsunami earthquake. *Journal of Geophysical Research: Solid Earth*, *120*, 1728–1747. <https://doi.org/10.1002/2014JB011721>
- Zhang, L., Wu, J. C., Ge, L. L., Ding, X. L., & Chen, Y. L. (2008). Determining fault slip distribution of the Chi-Chi Taiwan earthquake with GPS and InSAR data using triangular dislocation elements. *Journal of Geodynamics*, *45*(4–5), 163–168. <https://doi.org/10.1016/j.jog.2007.10.003>
- Zhou, F., & Shioya, T. (1996). Energy balance analysis on mode-III dynamic crack propagation in fixed sided strip. *International Journal of Fracture*, *80*(1), 33–44. <https://doi.org/10.1007/BF00036478>